ARCHIVES
OF CIVIL AND MECHANICAL
ENGINEERING

Original Research Article

Comparative analysis of numerical models of arch-shaped steel sheet sections

Artur Piekarczuk [a,*], Krzysztof Malowany [b]

[a] Building Research Institute, 1 Filtrowa St., 00-611 Warsaw, Poland
[b] Institute of Micromechanics and Photonics, Warsaw University of Technology, 8 Św. A. Boboli St., 02-525 Warsaw, Poland

ABSTRACT

The modern construction industry makes use of innovative production and assembly technologies, whose purpose is to implement reliable and simple structures. One product of such technologies is an arch-shaped steel sheet section that might be used as a self-supporting covering for general construction and industrial building construction. Considering complex geometry and boundary conditions, the FEM model of this structure is sophisticated and may contain errors. This paper presents numerical approaches for the calculation of sheet metal section elements of such coverings, namely two numerical approaches that differ in detailing of the properties of considered physical object. The first approach is based on a model that is characterized by simplified geometry and boundary conditions. The second scenario concerns a detailed FEM model with actual geometry captured by a laser triangulation method, experimentally determined material stress–strain relationship, and load conditions measured on an experimental stand. The results obtained with the use of computer simulations based on both approaches described above and experimental results are compared. The errors caused by simplification of the first numerical model are discussed. Finally, an acceptable reduction of FEM model complexity is proposed for the analyzed structure.

1. Introduction

Self-supporting arch-shaped covering structures originally served as temporary facilities for military and agricultural purposes. This covering type gained popularity mainly due to its simple design, quick installation and relatively low implementation costs compared to traditional types of covering structures (reinforced concrete, wood, and steel elements). Currently, this type of covering (the ABM 240 system) is used more and more often in the construction of public buildings. This technology is used to build coverings with spans ranging from 6 to 30 m with varying rise-to-span ratios [1]. The covering elements referred to as sections are fabricated on-site by the use of mobile rolling mills (Fig. 1), which form individual curved sections by
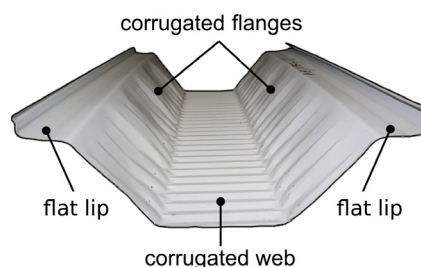

Fig. 1 – Section surfaces.

cold rolling from a single steel sheet (with a thickness of 0.7–1.5 mm).

Once formed, the section features the characteristic corrugated and wavy surfaces (Fig. 1). Individual sections are joined together by rolling down the free edges. The result is a curved surface constituting a self-supporting roof of the structure.

The existing calculation methods are based on the assumptions for steel bar structures analyzed in flat static systems [2–4]. For calculation of the structural components and stability, the following standards have been used: EN 1993-1-1 [5], EN 1993-1-3 [6], EN 1993-1-5 [7] and EN 1993-1-6 [8]. The normative documents present general principles for determining the load bearing capacity and stability, but they are not relevant to arch elements with a corrugated and wavy centre surface. Therefore, it is not possible to estimate the local loss of stability of a shell member with complex geometry. The height of the corrugation and waves of the centre surface of the section can be different depending on the bending radius of the arch and thus have a direct impact on the load bearing capacity and stability of the structure. The first pilot tests of full-sized arch-shaped elements of sheet metal sections were performed in the Building Research Institute [9]. The tests showed a strong impact of the local loss of load capacity on the stability and load capacity of the entire structural system. The mode of local stability loss of corrugated profiles subjected to axial and eccentric compression loads has been investigated in paper [10]. The results of numerical calculations and experimental tests were compared, and they showed a divergence between the results of the tests and those of the calculations due to the local loss of stability; in the presented study, the axial and compression stiffnesses of the tested profiles had not been taken into account. Similar studies were performed in papers [11,12]. These concerned the ABM 120 system. The study used point system measurement and numerical models with geometry created by scanning. The main difference was that the work of Walentynski et al. [11,12] did not take into account local strain measurements. Test results and calculations relate only to critical loads.

The main problem in implementing numerical analysis is the selection of a suitable shell model, which is a representation of the actual real-life working conditions of the system. This article describes the process of searching for the optimal model, taking into account the different levels of modelling precision and the adoption of boundary conditions. As a result of the process, information is obtained about possible errors of the systematic models. This information is useful for further work on full-sized modelling of covering elements and analysis of structures in real-life load conditions. In paper [13], a comparison between three different FEM models with simple boundary conditions and different levels of geometry simplification were performed, the model that gave results closest to the experimental ones was chosen for further analysis. The article presents the impact of selected modelling parameters on computational results using two numerical model: the first from the previous study [13]; and the second with actual geometry captured by a laser triangulation method, experimentally determined material models assigned to different regions of the structure, and load conditions measured on an experimental stand. The computational results will be compared with the available experimental results.

2. Assumptions

The computations and tests concern a section, which is a fragment of an arch-shaped covering fabricated using the ABM 240 technology. The assessment of simplified numerical models is presented in the article [13]. This article analyses three numerical section models that differed by the accuracy of geometry mapping. The models were assessed by comparing the calculation results with the test results. On the basis of the analysis, a single model that showed good similarity with the test results was selected. It can be assumed that the analysis described in the article [13] is an approximation of the modelling problem for a single reference value, i.e., the breaking force; however, it does not answer the question of how changes of individual parameters affect the computation result of the full range of reference value variation (a force of 0 to a destructive force). To fully compare the results of calculations, the simplified model selected in the article [13] was compared with the results of the model with perfectly mapped geometry, obtained as a result of 3D scanning. The difference between those two FEM models occurs also in boundary conditions, described in detail below.

In the article, two modelling scenarios are considered:

Scenario 1: The bilinear material model (referred to as the plastic web) is assumed on the basis of measuring the yield strength of the steel sheet prior to forming it into a section. After forming a section with the use of a rolling mill, the essential parameters of the geometry are measured (the parameters are marked in Fig. 9, and values are listed in Table 2), allowing for the creation of its own model. On this basis, a numerical model is created in commercial software from ANSYS. The element load method is assumed, i.e., eccentric compression carried out by axial forced displacement as a single-parameter extortion and theoretical support conditions. On the basis of these data, numerical analysis is performed. The result of the computation is the value of the support reaction as a function of forced displacement.

Scenario 2: The numerical model is created by importing a 3D scan of the test item. This model contains all of the geometric details. The conditions for support and load, in the form of displacements and rotation angles of supports, are adopted (multi-parameter geometric extortions) from earlier tests performed and entered as forced in the computational
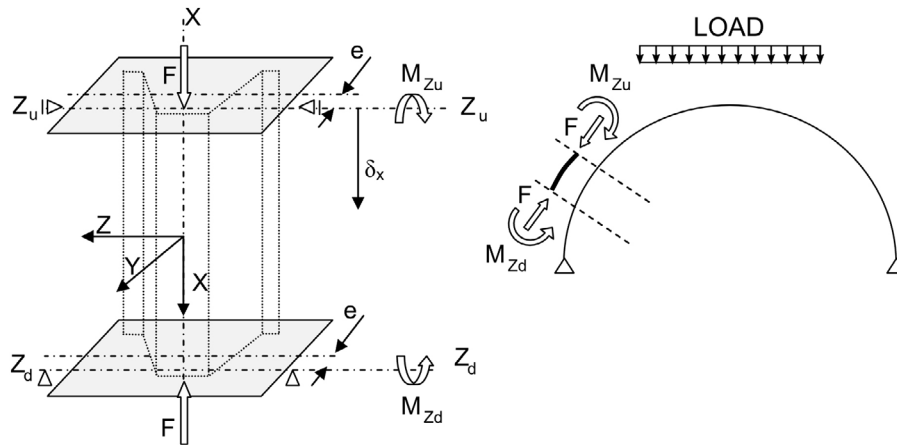
Fig. 2 – Test bench diagram [13].

model. The material model is adopted based on the measured strength properties of samples cut out from the element after the tests. The result of the computation is the value of the support reaction as a function of forced displacement.

It should be emphasized that Scenario 1 contains only vertical displacement as a load condition, in contrast to Scenario 2, which includes displacement and rotation, the same as in the test. Detailed data are summarized in Section 4.4. By comparing results of numerical analysis performed with the use of modelling approaches 1 and 2 against the test results, the model error is determined.

3. Tests

3.1. Tested specimens

The test piece is a section of the arch with a length of 1.0 m and a bending radius of 18 m, made of steel with a nominal thickness of 1.00 mm and the declared class S320GD+Z. The test bench design recreates the interaction of the other parts of the arch-shaped covering so that it maintains the section in a stable position and ensures transmission of internal forces according to the diagram of impacts of the remaining part of the arch. The X-axis is assigned to the specimens in such a way that it passes through the centre of gravity of cross sections, along the longitudinal axis. For test purposes, it was assumed that the load is applied to the

eccentricity (e), which in turn gives rise to the axial force (F), displacement (δ_x), and bending moment (M_{Zu}; M_{Zd}) (Fig. 2). This arrangement of forces corresponds to the actual distribution of forces in the cross-section of internal forces.

The tests of a section length were carried out on a test bench prototype (Fig. 3), which allows for axial and eccentric compression of the test piece. The load was carried out with the use of hydraulic cylinders, and the force was measured with the use of dynamometers coupled with a displacement measuring system. Measurement of displacement as a function of force was carried out continuously until the destruction of the sample.

The test piece (1) is mounted by means of screw connections in the top and bottom stabilization plates (2). The bottom plate is pin-supported. A pressure bar (3) is attached to the top plate, fitted with two dynamometers (4). Force is applied to the dynamometers through the use of a set of tendons and pulleys (5) fixed to hydraulic cylinders (5). The entire weight of the handles and the test piece is compensated by gravity through a set of weights (7) attached to the pressure bar. The measurement system (Fig. 4) consists of 8 inductive sensors, which are marked in the drawing with the symbols A1, A2, B1, B2, B3, B4, C1, and C2.

Sensors are used to measure the displacement X_1 of the upper stabilization plate and the rotation angles of the upper and lower plates: R_{x1}, R_{x2}, R_{y1}, R_{y2}, R_{z1}, R_{z2}. The test results are shown graphically in Fig. 5.
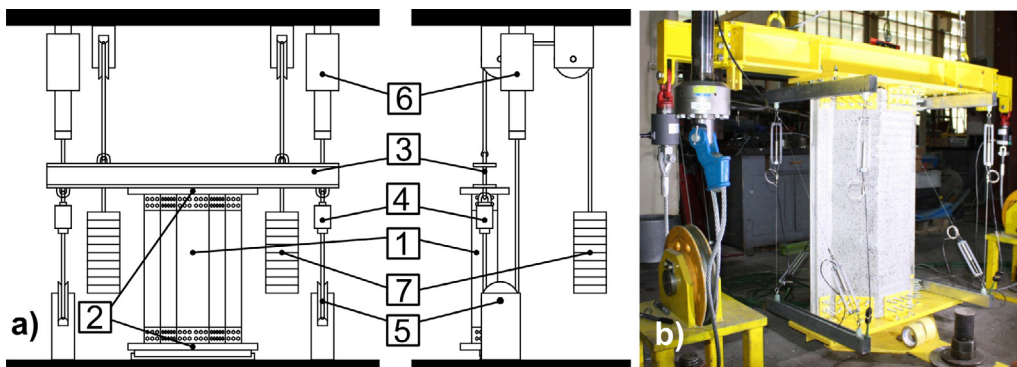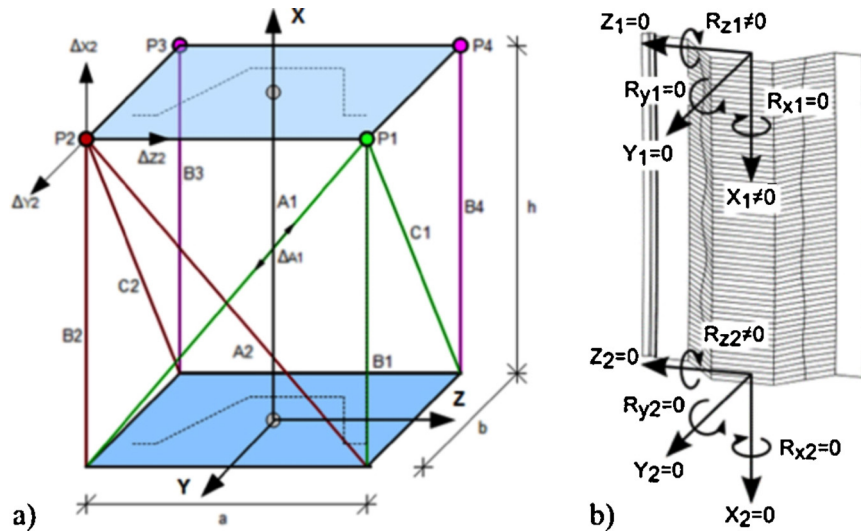

Fig. 3 – Test bench description [13].

Fig. 4 – The measuring system and determination of the measured values, (a) the measuring system, (b) determination of displacements and rotations.
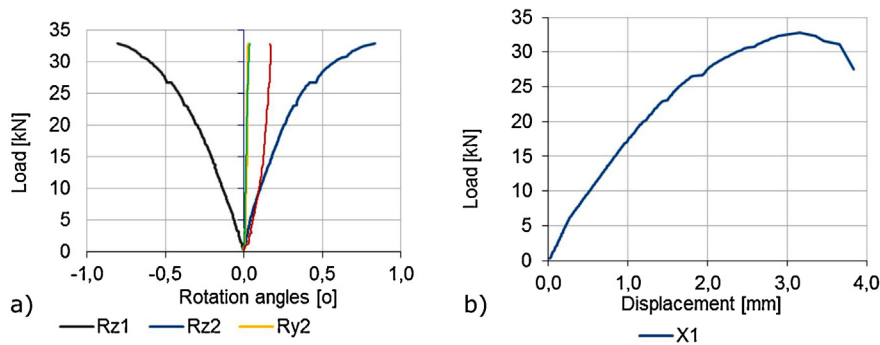

Fig. 5 – Measurement results, (a) the angles of rotation, (b) displacement along X_1 axis.

3.2. *Material testing and material stress–strain relationship*

The purpose of the test is to determine the actual yield strength and ultimate strength of the test pieces in accordance with EN ISO 6892-1:2009 [14]. Other properties, such as the longitudinal elastic modulus and Poisson's ratio, are adopted in accordance with the standards [5]. On the basis of the test results, a material model will be developed for adoption in the numerical computation. The method for testing the properties of the materials is described in scenarios 1 and 2 (item 2). They include the following:

Scenario 1: Base material tests. Samples were cut out from a flat metal sheet prior to the formation of the section. At this stage, 30 static tensile tests were carried out.
Scenario 2: Testing the material cut out from the test piece. Samples were taken from the three areas marked in Fig. 6.

Samples for the tests were collected from the test piece after tests from areas A, B, and C, outside of the zone of local loss of stability. Area (A) includes the central part of the corrugated surface, area B includes the wavy and corrugated webs, and area (C) refers to the web parts with longitudinal
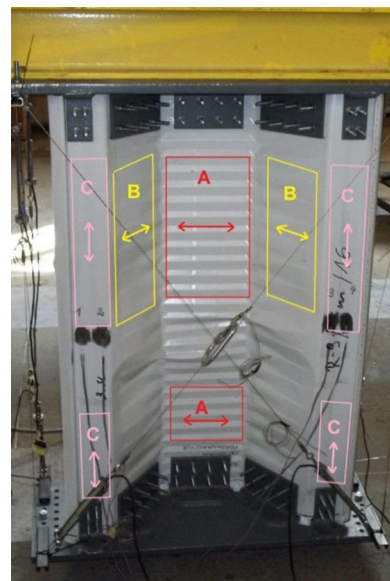

Fig. 6 – Areas and directions of sampling.

Table 1 – The results of the static tensile test.			
Scenario 1	Scenario 2		
	Area A (corrugation)	Area B (waves)	Area C (flat)
R_e = 366.3 MPa	R_e = 353.9 MPa	R_e = 374.0 MPa	R_e = 351.8 MPa
R_m = 383.6 MPa	R_m = 399.4 MPa	R_m = 391.4 MPa	R_m = 393.5 MPa

ribbing but without corrugation. The direction of sampling in various areas is shown by arrows in Fig. 6. The results of the static tensile tests (average values) in terms of yield strength (R_e) and ultimate strength (R_m) are summarized in Table 1.

The test results were assessed statistically. The purpose of the assessment was to determine whether the test results obtained for sheet samples in areas A, B, and C (scenario 2) did not differ statistically from the results of the flat sheet (scenario 1). To verify the normality of the distribution of the test results, the Shapiro–Wilk test was used for the flat sheet tests (30 trials). The hypothesis of the normal distribution of the results has been confirmed. Further analysis included test results of samples from areas A, B, and C. Test statistics were applied for the average values of Student's t-distribution with and without the assumption that the variances are equal in populations. On the basis of the analyses, it was demonstrated that the test results of samples from areas A, B, and C are significantly different from the results obtained from the flat sheet tests. It was found that, statistically, the results of the samples from areas A, B, and C also differ from each other. This means that the results of the series of 30 flat sheet tests cannot be used as the basis of the development of a material model that will be used in the calculation of geometric models in accordance with scenarios 2. A single model of the material behaviour to be used in the modelling approach 2 also cannot be used. Therefore, different material models were subsequently developed. The results of this work are presented in Section 4.1.

4. Numerical analysis

4.1. Material stress–strain relationship

In scenario 1, a steel stress–strain relationship is assumed to be of elastic–plastic nature with a nominal plateau slope in accordance with [7]. Fig. 7 shows a bilinear model with a solid

line and the averaged measurement result of 30 static tensile tests (scenario 1) with a dotted line. The graphical representation of the material model is shown on a scale of strain limited to 0.02%.

Next, the stress–strain relationship has been entered into the Engineering Data Sources module of the ANSYS system [15], into bilinear isotropic hardening.

In scenario 2, the stress–strain relationship adopted for numerical analysis with the use of the ANSYS programme [15] was developed in co-ordinates σ_{true}–ε_{ln}. The steel material properties are adopted as true stress–strain curve modified on the basis of the test results as follows:

$$\epsilon_{ln} = \int_{l_0}^{l} \frac{dl}{l} = \ln\left(\frac{l}{l_0}\right) = \ln\left(\frac{l_0 + \Delta l}{l_0}\right) = \ln\left(1 + \frac{\Delta l}{l_0}\right)$$
$$= \ln(1 + \epsilon_{eng}) \tag{1}$$

$$\sigma_{true} = \sigma_{eng}(1 + \epsilon_{eng}) \tag{2}$$

where ε_{ln} – logarithmic strain, σ_{true} – true stress, σ_{eng} – engineering stress (test result), ε_{eng} – engineering strain (test result), Δl – increase in the sample length [mm], l_0 – initial sample length [mm].

Stress–strain relationship is determined separately for each location on the surface of the section, i.e., areas A (corrugation), B (waves), and C (flat) according to the marks in Fig. 6. A graphical representation of the stress–strain relationship with a scale of strain limited to 0.02% with respect to the test results is shown in Fig. 8. Next, the numerical material stress–strain relationship will be implemented in the module Engineering Data Sources of the ANSYS system, into multilinear isotropic hardening.

The material models were assigned to areas corresponding to the sampling point for strength tests. A graphical representation of the areas with the assigned material model is presented in Fig. 11(b).
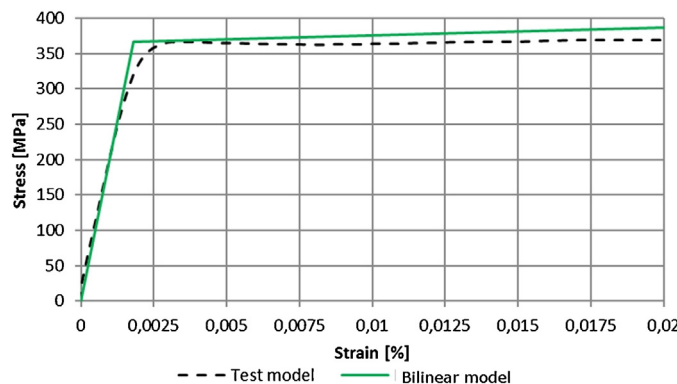

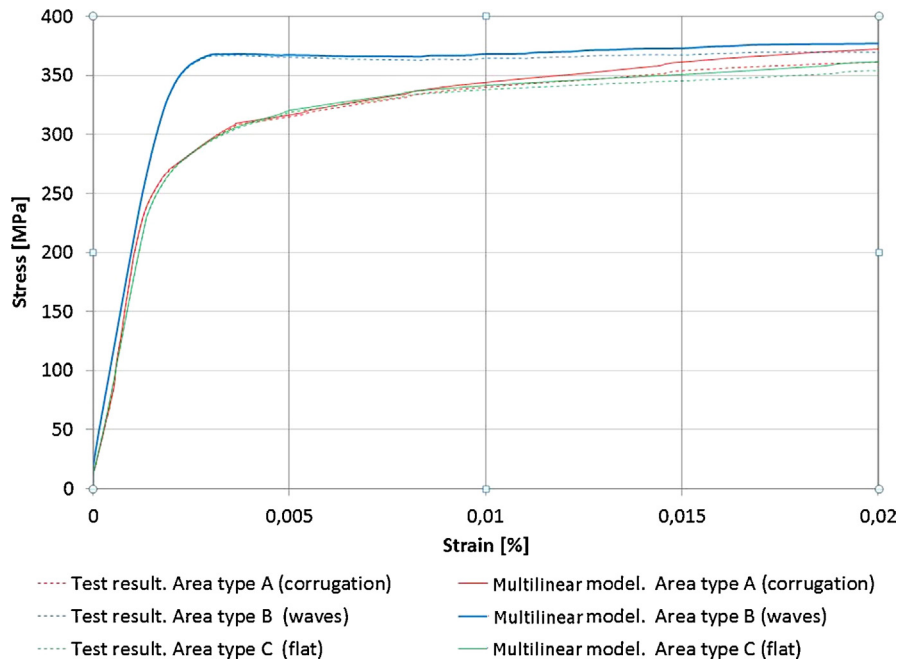Fig. 7 – Material model – Scenario 1.

Fig. 8 – Material model area A (corrugation), B (waves), and C (flat) – Scenario 2.
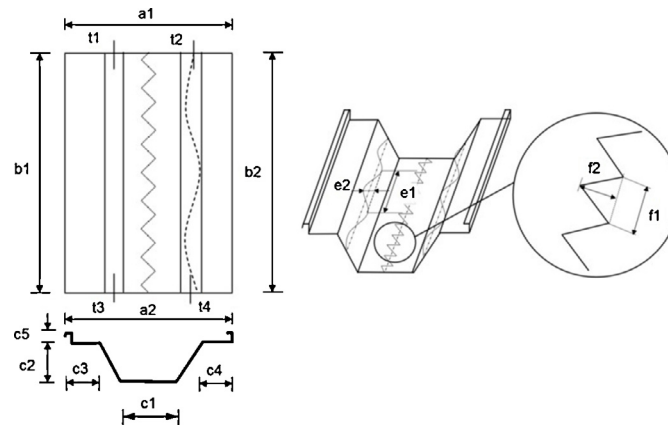

Fig. 9 – Sample view and explanation of symbols used in Table 2 [13].

4.2. Preparation of the geometric data for models

Two models were prepared for computation. The first model (scenario 1) was developed on the basis of the measurement of the test piece and entered into the Workbench module of the ANSYS programme. Geometric data were obtained from the test piece measurements. The identification of dimensions is shown in Fig. 9, and the measurement results are provided in Table 2.

The model includes the corrugation of the central part of the section (sector A), the corrugation and waving of the webs (sector B) and the non-ribbed portions of the webs with the bends (sector C). The longitudinal axis is curved on the arch with a radius of 18 m. The model assumes simplifications, which consist of the omission of bend radii on the border between sectors A, B and C. The longitudinal ribbing on the surface of sector C was also disregarded.

The geometry of the section of profiled steel sheets (second model – scenario 2) was obtained with the use of a handheld

scanner, the Nikon ModelMaker MMCx, mounted on 7-axis articulated arm, the Nicon MCAx [16] (Fig. 10). The measurement is based on a laser triangulation method, with the measurement accuracy equal to ±0.1 mm. The obtained geometry is represented as a point cloud, which was loaded into the FEM model.

4.3. Selection of finite elements

In models implemented in scenarios 1 and 2, Shell 281-type elements, shell elements with 8 nodes and six degrees of freedom at each node (three degrees of freedom of displacement and three degrees of freedom of rotation), were used with a quadratic interpolation function [17]. The parameters of the model meshing implemented in scenarios 1 and 2 are summarized in Table 3.

The parameter element quality (EQ) concerns the quality of the finite element mesh. This parameter is in the range

Table 2 – Actual dimensions of the sample (all values are given in mm).															
Width and height of web and flanges									Depth and length of the wave		Depth and length of corrugation		Sheet thickness		
a1	a2	b1	b2	c1	c2	c3	c4	c5	e1	e2	f1	f2	t1	t2	t3	t4
679	659	1018	1015	203.1	169.1	109.9	102.4	26.6	242.1	8.83	34.5	2.73	0.95	0.95	0.95	0.95

Fig. 10 – Geometry measurements of the section of profiled steel sheets.

between 0 and 1, where the value of 0 for the surface area (2D) is defined as an element of poor quality, and the value of 1 denotes a very good mesh. The parameter aspect ratio in the surface arrangement (2D) is defined as the ratio of the longest side to the shortest side of the finite element. The best parameters of the mesh are when the AR coefficient achieves the value of 1.0. Detailed rules for the determination of these

parameters are given in [17]. To evaluate the relationship of qualitative models, a reference level was adopted for the finite element mesh created for Model 2 (the 3D scan). For Model 1, the numbers of elements and nodes were selected in such a way that the discrepancy in relation to the reference model was not greater than 0.5%. EQ and AR parameters are close to 1, which means that the mesh elements are of good quality.

4.4. Conditions for support and load

The upper and lower supports are provided by a type of remote displacement [17] that maintains the Rigid-type relationship. This means that the degrees of freedom of displacement and rotation are associated with the central fulcrum in the local coordinate system. This method of support corresponds to fixing the rigid plate to the upper and lower edges of the section. The values of displacement and the angles of rotation may be released or forced.

Scenario 1 is computed with the assumption that the load is only a kinematic extortion by the displacement, which is applied to the upper support in the X-axis (axial displacement).

Scenario 2 is computed with the assumption that the load is a kinematic extortion by the displacement and the angles of rotation of the upper and bottom support. Extortion values are adopted from the tests. Table 4 presents a detailed description of the support and load conditions.

For the purpose of entering data load as boundary conditions (remote displacements) of the FEM model, the loads have been discretized into 10 intervals. Since scenario 1
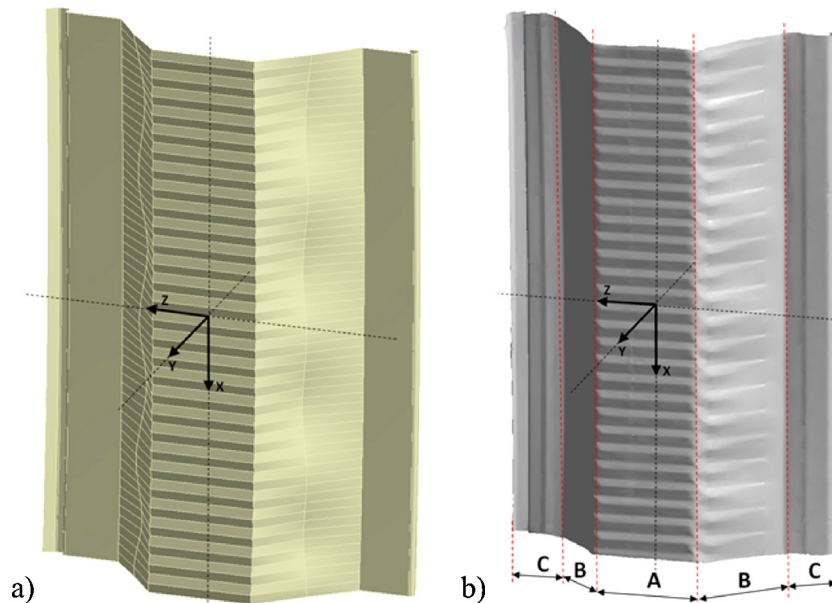

Fig. 11 – Numerical model of the section, (a) model 1 (created in ANSYS workbench), (b) model 2 (3D scan).
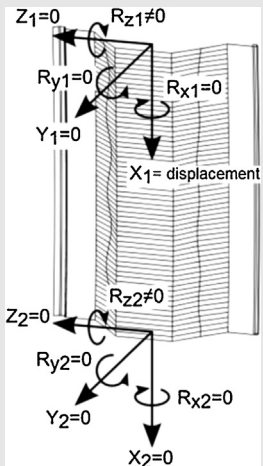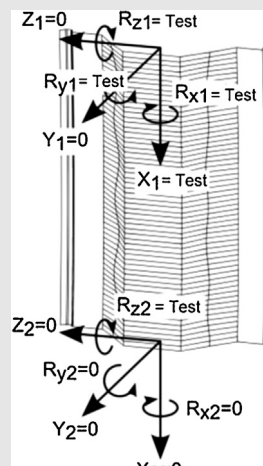
Table 3 – Finite element mesh parameters.

Scenario 1 (model 1)				Scenario 2 (model 2)			
N	E	EQ	AR	N	E	EQ	AR
172.903	57.329	0.988	1.075	172.686	57.567	0.951	1.174

N, number of nodes; E, number of finite elements; EQ, element quality; AR, aspect ratio.

Table 4 – Conditions for support and load.

Scenario 1		Scenario 2	
Top support	Bottom support	Top support	Bottom support
X_1 = displacement	$X_1 = 0$	X_1 = test	$X_1 = 0$
$Z_1 = 0$;	$Z_2 = 0$;	$Z_1 = 0$;	$Z_2 = 0$;
$Y_1 = 0$;	$Y_2 = 0$	$Y_1 = 0$;	$Y_2 = 0$
$R_{x1} = 0$;	$R_{y1} = 0$	R_{x1} = test	$R_{y1} = 0$
$R_{y1} = 0$;	$R_{y2} = 0$	R_{y1} = test	R_{y2} = test
$R_{z1} \neq 0$	$R_{z2} \neq 0$	R_{z1} = test	R_{z2} = test

assumes remote displacements in X_1 direction only, the extortion is composed of 10 equal sequences of displacement, with the value increasing from 0 to 3.0 mm in 0.3-mm intervals. In the scenario 2, the extortions are experimentally measured, therefore displacements and rotations obtained from the tests were discretized into 10 intervals. The discretization of displacements and angles of rotation of supports is presented in Fig. 12. The solid lines show the test results, and the points on the lines are data discretely assigned to 10 sequences.

The computation was performed using the arch-length approach with the full Newton–Raphson method [17].

4.5. Comparison between computational results

The results of the computations for the simplified model (scenario 1) and the scanned 3D model (scenario 2) are summarized in the following configurations:

- a graph showing the displacement–force (reaction) in the full load range with respect to the test and computational results,
- a graph showing the percentage discrepancy of the computational results with respect to the test results and

the mutual evaluation of the divergence of the numerical models,
- maps of reduced stresses, displacements and strains for the reaction peak value caused by the kinematic extortion of appropriate models,
- strain area maps with a size of 200 mm × 200 mm located in the central zone of the computational models.

The results of the analysis of the force as a function of vertical displacement are presented in Fig. 13. The force is obtained as a reaction to the actions of extortion kinematic.

In the graph, the peak forces and the corresponding displacements are identified. The peak force is reached when the strength limit of the element is achieved. When this value is exceeded, the test piece and the computational models lose their stability (falling curve). Table 5 summarizes the tests and computational results, which contain the peak values of forces and their corresponding axial displacements.

Because it is difficult to quantitatively evaluate the deviation of the computational results from the test results for each load level in Fig. 13, the test and computational results are presented in a unified data system for further analysis.
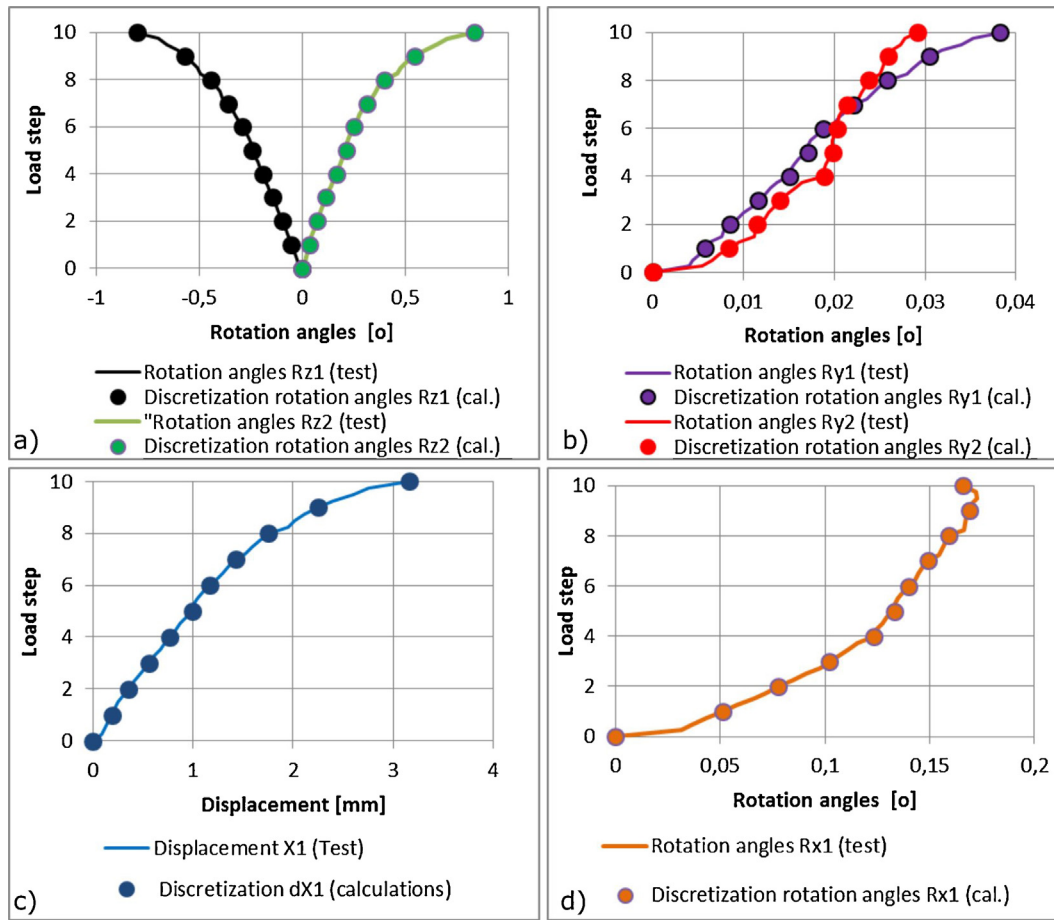
Fig. 12 – Test results and discretization of data in the scale of 10 sequences of extortions (test): (a) rotation angles of the top and bottom support with respect to the z-axis, (b) rotation angles of the top support with respect to the X-axis, (c) displacement of the top support along the X-axis, and (d) rotation of the top support with respect to the X-axis.

Table 6 presents the percentage deviation of the computational models from the test results over the entire range of load, determined with the use of the formula:

$$\Delta_{\%,i} = \frac{F_{\text{test},i} - F_{\text{cal},i}}{F_{\text{test},i}} \cdot 100 \, [\%] \tag{3}$$

where $F_{\text{test, }i}$ – test result presented as a reaction initiated by kinematic extortion on the ith step (i = 1, 2, …, 10), $F_{\text{cal, }i}$ – computational result presented as a reaction initiated by kinematic extortion on the ith step (i = 1, 2, …, 10).

A load step shall be understood as a conventional analysis interval used by the ANSYS software, in which a change in the kinematic conditions occurs (see Section 4.4). Table 6 shows the percentage divergences in the entire range of the analysis.

Divergences in computational results with respect to tests in the initial stages of extortion increase, reaching approximately about 13%. In the subsequent steps, as extortion increases, the divergences decrease; in step 5 of the analysis, the computational and test results converge, which corresponds to the force of approximately 22.5 kN. Then, the discrepancy increases and, upon achieving the peak force values, reaches 1.07% for the scenario 2 and 5.52% for the scenario 1.

The computational results are shown as a map of displacements and stresses in Fig. 14. The figure shows the map of reduced stress and the map of axial displacement for reaction peak values caused by kinematic extortion. Additionally, a graph is presented that shows an increase in the reaction and an increase in the stress reduced as a function of the increase (10 steps) of the kinematic extortion. The computational results of the simplified model (scenario 1) indicate the symmetry of the stress and displacement maps. The effect of the simplifications is visible, especially in the transition area between the corrugation web and corrugation flanges (see Fig. 1). The force peak value in Fig. 14(b) is present in the plastic zone. As far as the computations of the 3D model (scenario 2) are concerned, maps at the peak force range of reduced stresses do not show large areas of stress increase as in the simplified model (scenario 1). This is due to the

Table 5 – Test and computation results in relation to the force peak value.

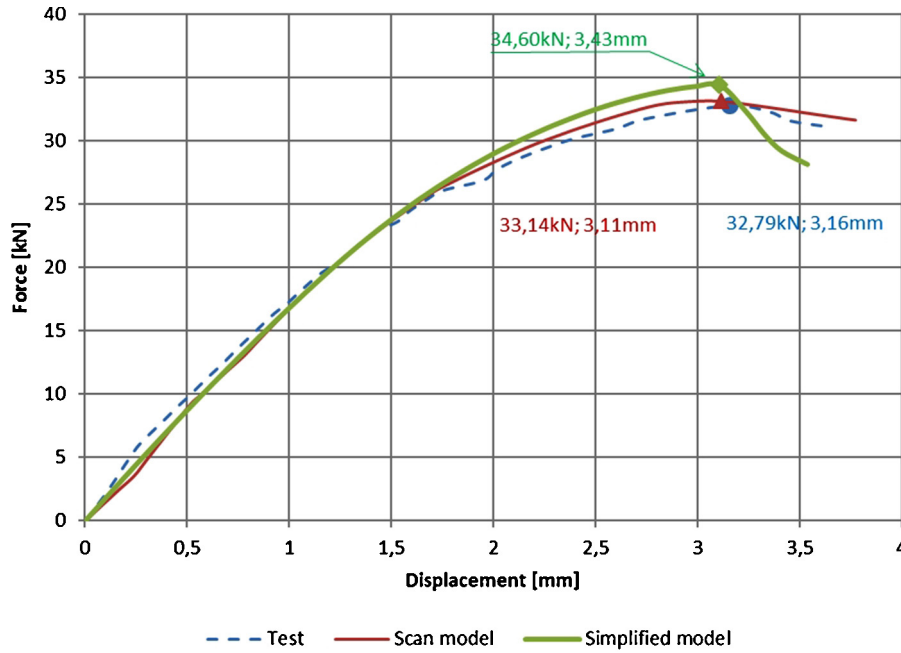|	Test model	Numerical model	
		Scenario 1	Scenario 2
Force [kN]	32.79	34.60	33.14
Displacement [mm]	3.16	3.43	3.11

Fig. 13 – The test and computational results in the coordinate system of force–displacement.

redistribution of stresses in the area of curvature, i.e., the transition of the corrugated and wavy surfaces (areas A and B, Fig. 11b). The map of axial displacement is asymmetric, which means that the computational result is affected by additional kinematic extortion conditions (rotation of the top support; see Table 4). The peak reaction value obtained in the 3D model computation (scenario 2) is in the plastic zone (Fig. 14e), as in the simplified model. In this case, the stress curve as a function of the increase in kinematic extortions has a different nature than in the simplified model. This is due to the use of three material models assigned to the corresponding cross-sectional areas (description item 4.1). In both computational scenarios, the elastic working range of the system is exhausted at a relatively early stage of the load, i.e., at a force of approximately 8 kN, which is approximately 25% of the maximum reaction.

Validation of the numerical models was performed with the utilization of data obtained from the 3D DIC method

[9,13,18]. The DIC 3D method works in full-field and, in experimental data, provides much more information than point-wise techniques. The measurements of displacements are simultaneously performed in all three directions for thousands or millions of points. In-plane strains (ε_{xx}, ε_{zz} – strains along x and z coordinates) are calculated from displacements using the following equations [18]:

$$\epsilon_{xx} = \frac{\partial u}{\partial x} + \frac{1}{2}\left[\left(\frac{\partial u}{\partial x}\right)^2 + \left(\frac{\partial w}{\partial x}\right)^2\right]$$
$$\epsilon_{zz} = \frac{\partial w}{\partial z} + \frac{1}{2}\left[\left(\frac{\partial u}{\partial z}\right)^2 + \left(\frac{\partial w}{\partial z}\right)^2\right]$$

(4)

In paper [13] the measurements of section of arch-shaped steel sheets with utilization of 3D DIC method are presented. The resulting displacement maps, obtained over the entire sample surface, have been used for the purpose of qualitative validation of FEM model, estimated accuracy of displacement

Load step	Test	Scenario 2	Scenario 1	Scenario 2	Scenario 1
	F_{test} [kN]	$F_{cal,2}$ [kN]	$F_{cal,1}$ [kN]	$\Delta_{\%2}$ [%] formula (3)	$\Delta_{\%1}$ [%] formula (3)
0	0	0	0	0	0
1.0	3.28	2.85	2.86	13.11	12.80
2.0	9.29	8.38	8.43	9.80	9.26
3.0	14.49	13.54	13.64	6.56	5.87
4.0	18.93	18.27	18.43	3.49	2.64
5.0	22.66	22.47	22.73	0.84	−0.31
6.0	25.72	26.08	26.45	−1.40	−2.84
7.0	28.16	29.02	29.54	−3.05	−4.90
8.0	30.03	31.21	31.91	−3.93	−6.26
9.0	31.36	32.58	33.49	−3.89	−6.79
10.0	32.79	33.14	34.60	−1.07	−5.52

Table 6 – Percentage differences between the test and the computational results.
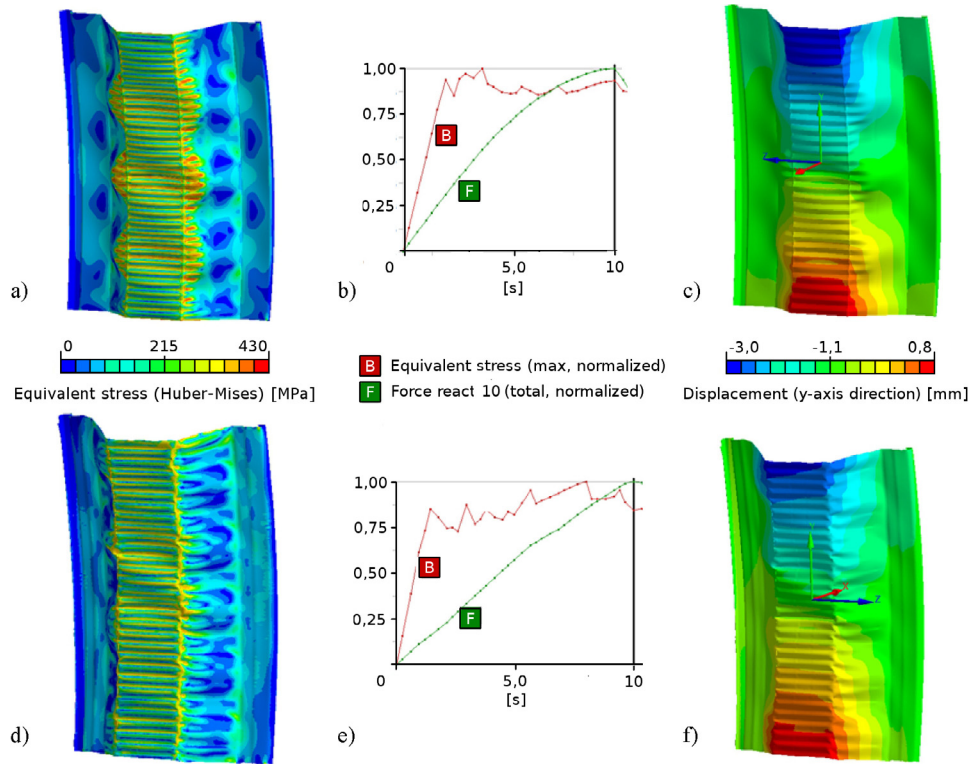
Fig. 14 – Computational results for peak load values, (a) reduced stress map – scenario 1 model, (b) reaction graph, stress as a function of the increase in extortion – scenario 1 model, (c) displacement map – scenario 1 model, (d) reduced stress map – scenario 2 model, (e) reaction graph, stress as a function of the increase in extortion – scenario 2 model, and (f) displacement map – scenario 2 model.

measurements was 20 μm. This accuracy was not suitable for determining accurate strain field distribution that would be used in further analysis. Therefore, in analysis presented in this paper, the area of interest was limited to the centre part of the measured sample. The area of interest (AOI) covers the area of 200×200 [mm^2] and is located in relation to the test piece as shown in Fig. 15. The obtained accuracy of displacement measurements was 5 μm. The measurement set comprises two Point Grey Grasshopper (2448×2048 pixels) monochromatic cameras equipped with 70-mm lenses, set at an angle of 30° and pointing to the same AOI of the specimen (Fig. 15). Measured displacements contain two components, the displacement of the sample and the random displacement of the stabilization plates (the bottom stabilization plate was placed on a bearing).
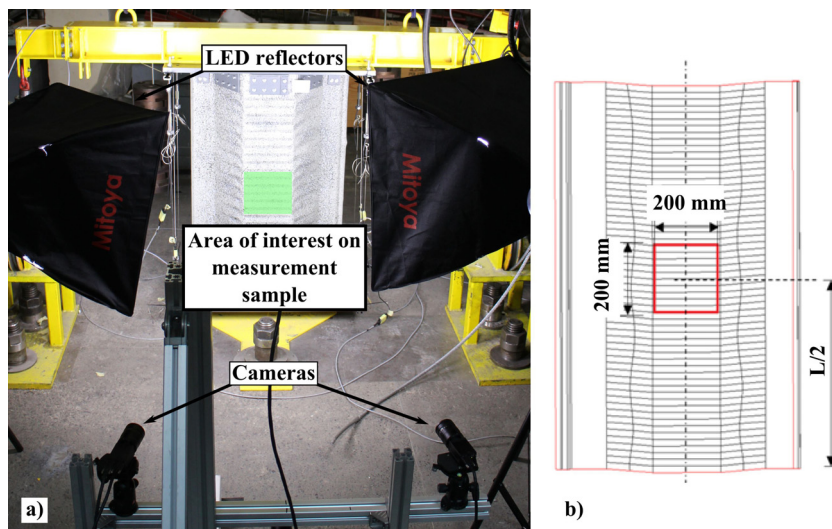

Fig. 15 – (a) Photo of the measurement system based on 3D DIC, (b) technical drawing of the measured sample–front view. Location of the area of interest, is marked on both images, in the picture (a) by green highlight, in the picture (b) by red border.
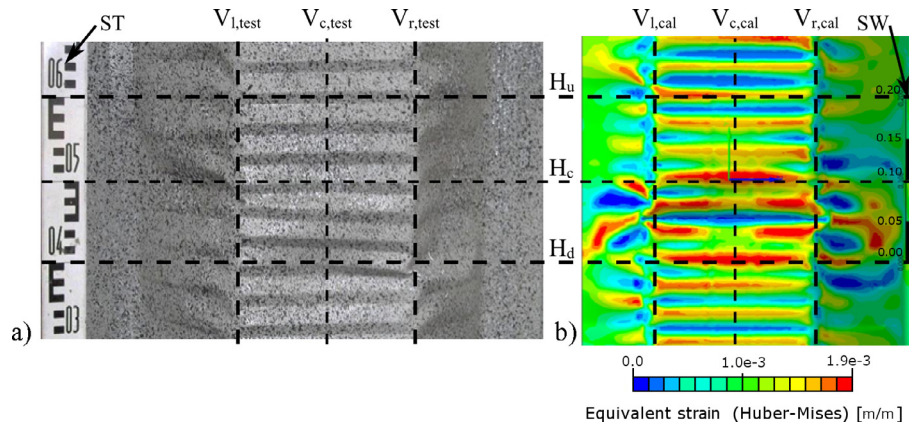
Fig. 16 – Detailed location of the strain observation area, (a) test piece, (b) computational model.
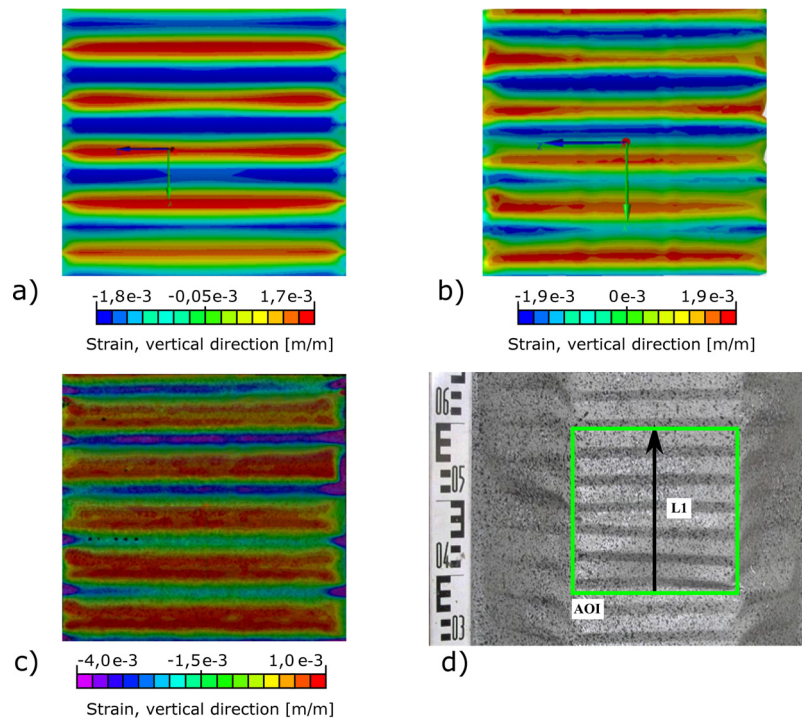

Fig. 17 – In the pictures areas covering the AOI of 3D DIC analysis are presented: (a) map of elastic strains (X direction) at the peak load value for the scenario 1; (b) map of elastic strains (X direction) at the peak load value for scenario 2; (c) experimental map of the strains (X direction); (d) section of the sample with the black lines marked L1, indicating the position of the cross-section analyzed in Fig. 18.

The displacements of stabilization plates can be treated as rigid body movements, which do not influence the strain calculation of the 3D DIC algorithm. Therefore, for the purposes of validating the numerical models, the obtained strain maps were used.

For the purpose of determining the quantitative and qualitative divergences in the computational results with respect to the strain area, the central area was selected for computational models. The detailed location of the field of observation of Huber–Mises strains is shown in Fig. 16. The horizontal lines indicate the top (H_u), the bottom (H_d) border area and the axial location of the field (H_c) of the area. The vertical lines indicate the left and right vertical boundaries and

the axial location of the field of the observation area for the test piece ($V_{L,test}$, $V_{r,test}$, $V_{c,test}$), and a similar definition is true for the area in the computational model ($V_{l,cal}$, $V_{r,cal}$, $V_{c,cal}$).

The measured sample is corrugated in the X direction, and therefore the strains in the X direction are considered in the following analysis. In Fig. 17a–c, the maps of elastic strains of scenarios 1 and 2 at the peak load value are compared to measure the strain map at maximum load in the AOI. In order to quantitatively compare the results, the profile L (Fig. 17d) of strains ε_{xx} is presented in Fig. 18.

The values of minimum and maximum elastic strains for the 90% of the maximum load ($0.9F_{max}$) fall in the following ranges:
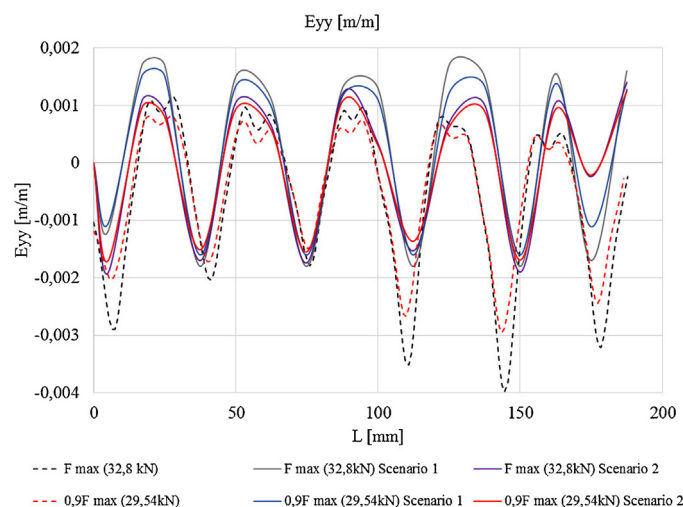
Fig. 18 – Strains in the X direction at points along line L1.

- $\varepsilon_{yy,\,max} = 0.0015$ m/m; $\varepsilon_{yy,\,min} = -0.0016$ m/m; scenario 1
- $\varepsilon_{yy,\,max} = 0.0012$ m/m; $\varepsilon_{yy,\,min} = -0.0017$ m/m; scenario 2
- $\varepsilon_{yy,\,max} = 0.0008$ m/m; $\varepsilon_{yy,\,min} = -0.0029$ m/m; test DIC

The values of maximum and minimum elastic strains for the max load (F_{max}) fall in the following ranges:

- $\varepsilon_{yy,\,max} = 0.0017$ m/m; $\varepsilon_{yy,\,min} = -0.0018$ m/m; scenario 1
- $\varepsilon_{yy,\,max} = 0.0019$ m/m; $\varepsilon_{yy,\,min} = -0.0019$ m/m; scenario 2
- $\varepsilon_{yy,\,max} = 0.0011$ m/m; $\varepsilon_{yy,\,min} = -0.0039$ m/m; test DIC

The maps of elastic strains are of a similar nature and demonstrate the variability of direction in the corrugated area. Divergences of FEM models in strain limits for the two different scenarios are approximately 10%. Strain values along the line L have similar character for both numerical models. Strain values obtained from tests and numerical simulations converge (Fig. 18) for the force of $0.9F_{max}$, along the line L, in its part starting at 25 mm and ending at 100 mm (see Fig. 17). At the same part of line L, strain values convergence of the numerical simulations and experimental results for the peak force (F_{max}) decreases. For the part of line L starting at 100 mm, the strains obtained from the simulation and experiment differ considerably. Difference between the FEM analysis and experimental results increases further with the increase of the applied force, which may be associated with a local loss of stability in this area.

5.   Conclusion and further works

The analysis of arch-shaped covering sections is difficult as both an experimental test and a computational task because of the complex geometry and load conditions. The section geometry results from the conditions of forming by cold rolling, and loads are a representation of the work of a discrete piece of the self-supporting system of a roof covering. The tests concerned the impact of the geometrical parameters of complex numerical models of section and boundary conditions (the method of the model load on the material) on the searched value, which is the reaction of the kinematic extortion throughout the load range, i.e. from the zero starting point to the destruction of the test piece.

Two scenarios were analyzed. The first concerned a simplified geometry model (our own model), a single parameter extortion (axial displacement) and a bilinear material model. The second model was characterized by precisely mapped geometry obtained by 3D scanning, multi-parameter geometric extortions (axial displacements, angles of rotation of supports), which mapped the test conditions, and different material stress–strain relationship assigned to respective areas on the surface of the model. Computational models were compared with the test results in relation to the same parameter, i.e., the reaction resulting from kinematic extortions.

In the process of the analyses, it was demonstrated that the divergences of the test and computational results of the two models over the entire area of sought values vary within the range of 0.3% to 13%. At the peak load value, the model analyzed in scenario 1 shows a 5.5% divergence of computational results compared to the tests, and 1.1% in scenario 2.

When analyzing the selected displacement field, the computational results of both models are presented only with respect to the elastic strain. Plastic strains diverge considerably.

The strain results in the central 200 mm × 200 mm area being presented in the elastic range. The calculation results most similar to the measurements are those obtained from scenario 2. The results of the calculations in scenario 1 protrude from the others. The reason for this phenomenon may be dependent on the level of detail of material models and section geometries. The ability to assess the deformation in a defined area allows for determining the mechanism and causes of local instability.

In practical applications, the data adopted for the model analysis in accordance with scenario 2 are difficult to implement because some of them (kinematic parameters extortion, material data) are available only after laboratory

tests and after the application of a complex 3D geometry scanning process. The analysis in this case is of a cognitive nature and provides an answer to the question: ''how closely can modelling approach the actual test conditions?'' Preparing the model implemented in accordance with scenario 1 requires relatively few operations compared to the model of scenario 2. It is sufficient to correctly enter the geometry of the measurable section characteristics (overall dimensions, corrugation, and waves) on the basis of measurements with common instruments and perform verification of the properties of the output material (steel sheet before section mill rolling), adopting a simplified bilinear model of the material on this basis. In this case, some simplifications can be adopted, e.g., certain features of the section geometry can be ignored, and intervals and values of load values (kinematic extortions) can be assumed a priori. Such simplifications do not contribute to substantial errors (only the evaluation of a single parameter, the peak value of reaction and displacement, is affected).

By comparing the computation and test verification results, the ranges for model errors were determined in the full load area. It was demonstrated that some simplifications of the geometry, load conditions and material model implemented in scenario 1 do not significantly affect the result of computations. At the same time, the adopted simplifications significantly reduce the effort necessary to prepare the model.

In future, experimental and numerical studies will be performed on several segments' structure in the laboratory to investigate the global stability of the metal arch. Next, full-scale objects in real-life environments will be investigated and compared to the mathematical model to determine the effects of the actual conditions of the support and full load-bearing capacity and stability of the structure. For numerical studies, an FEM model prepared in accordance to scenario 1 will be used. The experimental studies will be performed with the DIC 3D method, customized for long-term measurements [19,20].

Acknowledgements

REFERENCES

[1] US Navy Course, Steel Builder, NAVEDTRA 14251, 2 (1996).
[2] Z. Kurzawa, K. Reszut, M. Szumigała, Stalowe konstrukcje prętowe. Część III Konstrukcje z łukami, elementy cienkościenne, przekrycia membranowe, elementy zespolone, belki podsuwnicowe., Wydawnictwo Politechniki Poznańskiej, Poznań, 2015.
[3] A. Biegus, D. Czepiżak, Evaluation of resistance of corrugated sheets under bending by a concentrated loads from the local suspensions, Archives of Civil Engineering (2010) 283–297.
[4] J. Bródka, M. Broniewicz, M. Giżejowski, Kształtowniki gięte: poradnik projektanta, Polskie Wydawnictwo Techniczne 1 (2006) 105–110.
[5] EN 1993-1-1 Eurocode 3: Design of steel structure. General rules and rules for buildings
[6] EN 1993-1-3 Eurocode 3: General rules – Supplementary rules for cold-formed members and sheeting.
[7] EN 1993-1-5: Eurocode 3: General rules – Plated structural elements.
[8] EN 1993-1-6: Eurocode 3: Design of steel structures – Part 1–6: Strength and stability of shell structures.
[9] A. Piekarczuk, M. Malesa, M. Kujawinska, K. Malowany, Application of hybrid FEM-DIC method for assessment of low cost building structures, Experimental Mechanics 52 (2012) 1297–1311. , http://dx.doi.org/10.1007/s11340-012-9616-2.
[10] L.L. Wu, Y.J. Shi, Theoretical and experimental study on interactive local buckling of arch-shaped corrugated steel roof, International Journal of Steel Structures 6 (2006) 45–54.
[11] R. Walentynski, M. Cybulski, R. Cybulski, Influence of geometric imperfections on the local stability of thin-walled elements, Shell Structures: Theory and Applications 3 (2013) 251.
[12] R. Cybulski, R. Walentyński, M. Cybulska, Local buckling of cold-formed elements used in arched building with geometrical imperfections, Journal of Constructional Steel Research 96 (2014) 1–13. , http://dx.doi.org/10.1016/j.jcsr.2014.01.004.
[13] A. Piekarczuk, K. Malowany, P. Więch, M. Kujawińska, P. Sulik, Stability and bearing capacity of arch-shaped corrugated shell elements: experimental and numerical study, Bulletin of the Polish Academy of Sciences Technical Sciences 63 (2015), http://dx.doi.org/10.1515/bpasts-2015-0013.
[14] EN ISO 6892-1:2009: Metallic materials – Tensile testing – Part 1: Method of test at room temperature.
[15] J. Świniarski, M. Królak, K. Kowal-Michalska, Schematyzacja charakterystyki materiału a charakterystyka rzeczywista w analizie porównawczej modelu MES i badań doświadczalnych stateczności dźwigarów cienkościennych, Acta Mechanica et Automatica 2 (1) (2008) 73–76.
[16] http://www.nikonmetrology.com/en_EU/Products/Portable-Measuring (01.10.2015).
[17] P. Kohnke (Ed.), Theory Reference for the Mechanical APDL and Mechanical Applications, Ansys Inc., USA, 2009.
[18] M.A. Sutton, J.-J. Orteu, H. Schreier, Image Correlation for Shape, Motion and Deformation Measurements: Basic Concepts, Theory and Applications, 1st ed., Springer Publishing Company, Incorporated, 2009.
[19] M. Malesa, M. Kujawinska, Modified two-dimensional digital image correlation method with capability of merging of data distributed in time, Applied Optics 51 (2012) 8641, http://dx.doi.org/10.1364/AO.51.008641.
[20] M. Malesa, M. Kujawinska, Deformation measurements by digital image correlation with automatic merging of data distributed in time, Applied Optics 52 (2013) 4681, http://dx.doi.org/10.1364/AO.52.004681.